

Published in final edited form as:

*Neuroimage*. 2013 February 15; 67: 193–202. doi:10.1016/j.neuroimage.2012.10.050.

## Imaging neural architecture of the brain based on its multipole magnetic response

Chunlei Liu<sup>a,b,\*</sup> and Wei Li<sup>a</sup>

<sup>a</sup>Brain Imaging and Analysis Center, School of Medicine, Duke University, Durham, NC, USA

<sup>b</sup>Department of Radiology, School of Medicine, Duke University, Durham, NC, USA

### Abstract

Although magnetic fields interact weakly with biological tissues, at high fields, this interaction is sufficiently strong to cause measurable shifts in the Larmor frequency among various tissue types. While measuring frequency shift and its anisotropy has enabled NMR spectroscopy to determine structures of large molecules, MRI has not been able to fully utilize the vast information existing in the frequency to elucidate tissue microstructure. Using a multipole analysis of the complex MRI signal in the Fourier spectral space, we developed a fast and high-resolution method that enables the quantification of tissue's magnetic response with a set of magnetic susceptibility tensors of various ranks. The Fourier spectral space, termed **p**-space, can be generated by applying field gradients or equivalently by shifting the **k**-space data in various directions. Measuring these tensors allows the visualization and quantification of tissue architecture. We performed 3D whole-brain multipole susceptibility tensor imaging in simulation, on intact mouse brains *ex vivo* and on human brains *in vivo*. We showed that these multipole susceptibility tensors can be used to image orientations of ordered white matter fibers. These experiments demonstrate that multipole tensor analysis may enable practical mapping of tissue microstructure *in vivo* without rotating subject or magnetic field.

### Keywords

MRI; Magnetic susceptibility anisotropy; Susceptibility tensor imaging; Brain connectivity; **p**-space

### Introduction

Magnetic fields can penetrate deep into the body since they interact with biological molecules weakly as evidenced by the routine application of MRI in human bodies. Because of this weak interaction, MRI has traditionally relied on the amplitude of the nuclear magnetization from the very beginning to generate tissue contrast (Lauterbur, 1973). However, at high fields, interaction between magnetic field and the orbital electrons of biomolecules may introduce a measurable perturbation on the resonance frequency of surrounding water protons. This perturbation in turn reflects the molecular content and microstructure of the tissue. A notable example is the relative frequency shift between gray and white matter and between layers of the cortex which is thought to originate from variations of magnetic susceptibility (Duyn et al., 2007; Rauscher et al., 2005). Although

frequency shift has provided a new image contrast for MRI, utilizing this contrast to infer neural architecture and brain structural connectivity remain challenging.

One potential way to fully utilize this frequency is to borrow techniques from NMR spectroscopy. Indeed, measuring frequency shift has been instrumental in NMR spectroscopy for probing molecular structure. While high-resolution NMR techniques provide a wealth of information (de Beer et al., 1994; Otting et al., 1990; Tolman et al., 1995; van Zijl et al., 1984), adapting those techniques to high-resolution imaging is not yet possible. The difficulty is partially due to low sensitivity, limited scan time and vastly more complex physiological conditions encountered in volumetric brain imaging. Because of these difficulties, frequency shift measured by MRI has been limited to the zero-*th* order information, i.e. the mean frequency of a whole voxel (Dixon, 1984; Glover and Schneider, 1991; Haacke et al., 1995; Rauscher et al., 2005; Weisskoff and Kiihne, 1992). Higher-order information such as susceptibility anisotropy of dipoles and quadrupoles, if resolved, would provide important information of sub-voxel tissue and cellular architecture. Similar to the important role that NMR has played in untangling molecular structure (Cavalli et al., 2007; Otting et al., 1990; Wishart et al., 1992), imaging higher-order frequency variation could provide a powerful tool for probing tissue microstructure such as brain connectivity noninvasively.

The backbone of brain connectivity is composed of bundled long projecting axons. Structurally, this connectivity backbone may be compared to the backbones of macromolecules. Ordered arrangement of atoms along the chain axis of macromolecules gives rise to an NMR measurable anisotropic susceptibility tensor. Similarly, on the tissue scale, the ordered arrangement of axon bundles also produces anisotropic frequency (He and Yablonskiy, 2009) and susceptibility (Lee et al., 2010; Li et al., 2012b; Liu, 2010). Although the mean susceptibility of a voxel can be measured with a gradient echo (de Rochefort et al., 2008; Li, 2001; Salomir et al., 2003), it does not measure the orientation dependence of the susceptibility (Li et al., 2011). To measure the anisotropy of magnetic susceptibility, the method of susceptibility tensor imaging (STI) has been used (Liu, 2010). A recent study also explored the capability of STI for tracking neuronal fibers in 3D in the mouse brain *ex vivo* (Liu et al., 2012). In large fiber bundles, the orientation determined by STI was found to be comparable to that by diffusion tensor imaging (DTI) of diffusion anisotropy (Basser et al., 1994, 2000; Moseley et al., 1990). However, this experimental procedure of STI requires rotating the object or the magnetic field. The requirement is clearly not convenient or even impractical for routine brain imaging on standard MRI scanners *in vivo*.

Here, we developed a method to measure higher-order frequency variations based on a single image acquisition without rotating the object or the magnet. This method utilized a multipole analysis of the MRI signal in a sub-voxel Fourier spectral space termed “**p**-space” for short. By sampling the **p**-space with pulsed field gradients or by shifted image reconstruction, we were able to measure a set of dipole and quadrupole susceptibility tensors. We illustrated the methodology in a simulation of aligned axons and demonstrated its use for 3D high-resolution imaging of mouse brains *ex vivo* at 9.4 Tesla and human brains *in vivo* at 3.0 Tesla. We anticipate that the **p**-space approach may provide a powerful method for studying tissue microstructure and brain connectivity *in vivo* and non-invasively.

## Methods

### The spectral space (**p**-space) of microscopic magnetic field

For a given imaging voxel containing heterogeneous structures, magnetic field within the voxel is also heterogeneous due to the interaction between tissue and external field. The total magnetization of the voxel is an integral of all spins within the voxel, each experiencing a

slightly different local magnetic field. The phase angle of the resulting integral represents the amplitude of the mean field. The spatial heterogeneity, however, is lost during the ensemble averaging. If the field distribution within the voxel can be recovered, it will allow us to infer the underlying tissue microstructure.

One way to recover the field distribution is to apply an external magnetic field gradient which will modulate the resonance frequency of the spins within the voxel. Specifically, given a voxel of width  $[v_1, v_2, v_3]$  centered at location  $\mathbf{r}$  in the laboratory's frame of reference, the field distribution within the voxel can be denoted as  $\mathbf{B}(\mathbf{r}+\mathbf{x})$ . Here,  $\mathbf{x}$  is the coordinate of a spin in the voxel's frame of reference whose origin is at the center of the voxel. Both  $\mathbf{r}$  and  $\mathbf{x}$  are normalized by the width of the voxel, thus dimensionless. In the presence of a pulsed field-gradient  $\mathbf{G}$ , the voxel-averaged MRI signal  $s(\mathbf{r})$  at time  $t$ , ignoring  $T_2$ -relaxation, is given by

$$s(\mathbf{r}) = \int_{\mathbf{x}} \rho(\mathbf{r}+\mathbf{x}) e^{-i\gamma \left( B_3(\mathbf{r}+\mathbf{x}) + \sum_{j=1}^3 G_j (r_j+x_j) v_j \right) t} d\mathbf{x} \quad (1)$$

Here,  $i$  is the imaginary number and the index  $j$  represents the three axes of a Cartesian coordinate system with (1, 2, 3) corresponding to  $(x, y, z)$  respectively.  $B_3(\mathbf{r}+\mathbf{x})$  is the  $z$ -component of  $\mathbf{B}(\mathbf{r}+\mathbf{x})$  which is along the direction of the  $\mathbf{B}_0$  field;  $\rho(\mathbf{r})$  is the spin density at position  $\mathbf{r}$  and  $\gamma$  is the gyromagnetic ratio. Eq. (1) can be rewritten as

$$s(\mathbf{r}) = e^{-i2\pi\mathbf{p}\cdot\mathbf{r}} \int_{\mathbf{x}} \rho(\mathbf{x}) e^{-i\gamma B_3(\mathbf{x})t} e^{-i2\pi\mathbf{p}\cdot\mathbf{x}} d\mathbf{x} \quad (2)$$

where  $\mathbf{p}$  is a dimensionless spatial frequency vector with  $p_j = \gamma G_j v_j t / 2\pi$ . The symbol  $\mathbf{r}$  has been dropped from the integral with the understanding that both  $\rho$  and  $B_3$  are expressed in the voxel's coordinate system. In other words, the magnetization is proportional to the Fourier spectrum of the complex magnetization distribution function. Herein, this spectral space will be referred to as the  $\mathbf{p}$ -space to differentiate it from the  $\mathbf{k}$ -space that is commonly used in image acquisition. The Fourier integral in Eq. (2) can be separated into magnitude  $m(\mathbf{r}, \mathbf{p})$  and phase  $\Phi(\mathbf{r}, \mathbf{p})$  as

$$s(\mathbf{r}) = e^{-i2\pi\mathbf{p}\cdot\mathbf{r}} m(\mathbf{r}, \mathbf{p}) e^{-i\Phi(\mathbf{r}, \mathbf{p})} \quad (3)$$

Both the magnitude and the phase are expected to depend on the applied field gradient. Notice that if the voxel is an ideal delta function, i.e.  $\rho(\mathbf{x}) e^{-i\gamma B_3(\mathbf{x})t} = \delta(\mathbf{x})$ , then the integral in Eq. (2) will be always equal to 1 regardless of the  $\mathbf{p}$ -vector. In this extreme case, no additional information can be gained by applying field gradients. In reality, however, all imaging voxels have a finite dimension with a distributed magnetization. Sampling the  $\mathbf{p}$ -space will thus allow us to probe sub-voxel magnetization and magnetic field distribution.

### Multipole susceptibility tensors in the $\mathbf{p}$ -space

In a second-order multipole expansion (Jackson, 1975) (or Taylor's expansion in Cartesian coordinates) (Appendix A),  $\Phi(\mathbf{r}, \mathbf{p})$  can be written as

$$\Phi(\mathbf{p}) = \Phi_0 + \gamma B_0 t \widehat{\mathbf{p}}^T \chi_d \widehat{\mathbf{p}} + \gamma B_0 t \widehat{\mathbf{p}}^T \chi_g \widehat{\mathbf{p}} p^2 \quad (4)$$

In Eq. (4), the first term is the mean phase. The second term is a dipole moment in which  $\chi_d$  is a rank-2 dipole susceptibility tensor and  $\hat{\mathbf{p}}$  is the unit directional vector. The third term is a quadrupole moment expressed in terms of a rank-2 quadrupole susceptibility tensor  $\chi_q$ . More specifically,  $\Phi_0$  is the phase when no gradient is applied and it is related to the image-space dipole susceptibility tensor (rank 2)  $\chi(\mathbf{r})$  following (Liu, 2010)

$$\Phi_0 = \gamma t F T^{-1} \left\{ \frac{1}{3} \widehat{\mathbf{B}}_0 F T \{ \chi \} \mathbf{B}_0 - k_3 \frac{\mathbf{k}^T F T \{ \chi \} \mathbf{B}_0}{k^2} \right\} \quad (5)$$

Here,  $\widehat{\mathbf{B}}_0$  is a unit directional vector (dimensionless). The quadrupole tensor  $\chi_q$ , in its complete form, is a rank-3 tensor (Jackson, 1975). However, since  $\mathbf{B}_0$  is in the  $z$ -direction, the third dimension of  $\chi_q$  is locked to the  $z$ -direction, thus reducing it to a rank-2 tensor.

Similarly, the magnitude can be expanded as

$$m(\mathbf{p}) = m_0 \left( 1 + \gamma B_0 t \widehat{\mathbf{p}}^T \boldsymbol{\eta}_d \widehat{\mathbf{p}} + \gamma B_0 t \widehat{\mathbf{p}}^T \boldsymbol{\eta}_q \widehat{\mathbf{p}}^2 \right) \quad (6)$$

where both  $\boldsymbol{\eta}_d$  and  $\boldsymbol{\eta}_q$  are dimensionless rank-2 tensors. Given a set of  $\mathbf{p}$ -vectors, Eqs. (4) and (6) can be used to determine the multipole tensors.

### Measuring $\mathbf{p}$ -space susceptibility tensors

To measure  $\mathbf{p}$ -space multipole tensors, a standard gradient-echo sequence could be used with an added spectral sensitizing gradient (Fig. 1a). The spectrum-sensitizing gradient induces a shift in the  $\mathbf{k}$ -space. Utilizing this shifting effect, we achieved spectral weighting during image reconstruction by simply shifting the  $\mathbf{k}$ -space data with the desired  $\mathbf{p}$ -vector. This strategy allowed the sampling of the  $\mathbf{p}$ -space without applying physical gradients. By shifting the reconstruction window in various directions and with various distances, a series of images can be reconstructed (Fig. 1b). For each shift in the  $\mathbf{p}$ -space, a linear phase term is also added to the image as described in Eq. (2). This linear phase must be removed before calculating the phase spectrum (Fig. 1b).

The  $\mathbf{p}$ -space can be sampled in many different ways. If it is sampled on a spherical surface with a constant radius of  $p$ , the susceptibility tensors can be calculated by inverting the resulting system of linear equations defined by Eqs. (4) and (6). Alternatively, the  $\mathbf{p}$ -space can be sampled continuously along a given direction, thus allowing the calculation of the signal variation along that particular direction. If the maximal  $p$ -value along a unit-direction  $\hat{\mathbf{p}}$  is denoted by  $p_{\max}$ , the standard deviation of the dipolar phase is given by (Appendix B)

$$\delta\Phi_d = \frac{1}{\sqrt{3}} \gamma B_0 t p_{\max} \widehat{\mathbf{p}}^T \chi_d \widehat{\mathbf{p}} \quad (7)$$

The standard deviation of the quadrupolar phase is given by

$$\delta\Phi_q = \frac{2}{\sqrt{45}} \gamma B_0 t p_{\max}^2 \widehat{\mathbf{p}}^T \chi_q \widehat{\mathbf{p}} \quad (8)$$

The corresponding frequency terms can be calculated by dividing by  $2\pi t$ . The standard deviations of the magnitude are given similarly with  $\chi$  replaced by  $\boldsymbol{\eta}$ . Given a set of non-colinear directions, the susceptibility tensors can be calculated by inverting Eqs. (7) and (8).

Notice that there is a sign ambiguity when taking the square root of the variance. The choice of positive sign does not indicate whether the material is diamagnetic or paramagnetic as it is based on **p**-space moments rather than image-space susceptibility itself. A notable advantage of calculating the variance is that the absolute susceptibility tensors can be determined independent of the reference frequency.

### Numerical simulation

A cubic voxel packed with an ensemble of parallel axons was generated. The voxel had a dimension of  $d=256\ \mu\text{m}$  on all sides. The axons were aligned along the  $z$ -axis. The  $B_0$  field was parallel to the  $y$ - $z$  plane, tilted by  $50^\circ$  from the  $z$ -axis (Fig. 2a). The inner radius of the axon was  $3.5\ \mu\text{m}$  and the outer radius was  $5.0\ \mu\text{m}$ . The distance between two neighboring axons was uniformly distributed between  $11.0\ \mu\text{m}$  and  $12.5\ \mu\text{m}$ . The susceptibility of the axons was set to be  $-0.082$  ppm and the susceptibility anisotropy ( $\chi_{\parallel} - \chi_{\perp}$ ) of the myelin sheath was  $0.163$  ppm with  $\chi_{\parallel}$  being  $-0.1$  ppm (Li et al., 2012a). Here  $\chi_{\parallel}$  is defined as the susceptibility along the direction parallel to the axon. The susceptibility of the interstitial space was assumed to be zero as the reference. The voxel was divided into a  $512 \times 512 \times 512$  grid resulting in a grid size of  $0.5\ \mu\text{m}$ . A susceptibility tensor was assigned to each voxel depending on the tissue type. Only voxels within the myelin sheath had anisotropic tensors. The major eigenvectors of the myelin tensors were perpendicular to the long axis of the axon (Li et al., 2012a). The magnetic field at each voxel was computed *via* the forward Fourier relationship between susceptibility tensor and magnetic field as expressed in Eq. (5). The MR signal generated by the voxel was evaluated at  $TE=20$  ms. A total of 10,000 unit **p**-vector were generated that evenly cover the surface of a unit sphere. At each orientation, the **p**-space was sampled in 128 evenly spaced locations in the range of  $\pm 0.5$ . Gaussian noise was added in the real and imaginary part of the signal resulting in an SNR of 20. Along a given direction, the standard deviation was computed for both frequency and magnitude.

### MRI experiments

Adult 10-weeks old C57BL/6 mice ( $n=3$ , The Jackson Laboratory, Bar Harbor, ME) were anesthetized and perfusion fixed (Johnson et al., 2002). Brains were kept within the skull to prevent potential damages caused by surgical removal. Each specimen was sealed tightly inside a cylindrical tube (length 30 mm and diameter 11 mm). The tube containing the specimen was placed inside a tightly fitted solenoid radiofrequency coil constructed from a single sheet of microwave substrate. Images were acquired on a 9.4 T (400 MHz) 89-mm vertical bore Oxford magnet with shielded coil providing gradients of 2200 mT/m. The system is controlled by a GE EXCITE MR imaging console. A 3D spoiled-gradient-recalled-echo (SPGR) sequence was used with the following parameters: matrix size= $512 \times 256 \times 256$ , field-of-view (FOV)= $22 \times 11 \times 11\ \text{mm}^3$ , bandwidth (BW)=62.5 kHz, flip angle= $60^\circ$ ,  $TE=[4.4, 7.0, 9.0, 11.0, 13.0, 15.0]$  ms and  $TR=100.0$  ms. Scan time was 1 hour and 49 minutes. 3D Diffusion-weighted images were acquired using a pulsed-gradient spin-echo sequence at a  $b$ -value of  $1500\ \text{s/mm}^2$  and with six encoding directions ( $[1\ 1\ 0]$ ,  $[1\ 0\ 1]$ ,  $[0\ 1\ 1]$ ,  $[1\ -1\ 0]$ ,  $[1\ 0\ -1]$ , and  $[0\ 1\ -1]$ ). One non-diffusion weighted volume was also acquired in order to calculate the diffusion tensor with a standard linear fitting. The acquisition parameters were:  $TE=12$  ms,  $TR=700$  ms, matrix= $256 \times 128 \times 128$ ,  $FOV=22 \times 11 \times 11\ \text{mm}^3$ . Total scan time for DTI was 22 hours and 19 minutes.

Three healthy adult volunteers were scanned on a 3.0 T GE MR750 scanner (GE Healthcare, Waukesha, Wisconsin) equipped with an 8-channel head coil and a maximal gradient strength of 50 mT/m. Images were acquired using a 16-echo 3D SPGR sequence with the following parameters:  $FOV=192 \times 192 \times 120\ \text{mm}^3$ , matrix size= $192 \times 192 \times 120$ , BW=62.5 kHz, flip angle= $20^\circ$ ,  $TE$  of the first echo= $4.0$  ms, echo spacing= $2.3$  ms and  $TR=50.0$  ms. Total scan time was 19.2 minutes. A 3D volume of inversion-recovery prepared T1-weighted

images were also acquired for anatomical reference. The study was approved by the Institutional Review Board.

### p-Space data analysis

A total of 213 orientations in the **p**-space were sampled. For the convenience of data shifting, these directions were expressed in signed integer numbers as  $[n_1 \ n_2 \ n_3]$  without normalization. The maximal number used was 5. Raw images were first zero-padded to a cubic  $N \times N \times N$  matrix ( $N=512$  for mouse and 192 for human), thus identical FOV in all three dimensions. This operation resulted in isotropic resolution in both the **k**-pace and the image domain. The **k**-space data were then shifted by a given **p**-space vector. Data shifted outside the prescribed matrix were discarded, while new locations were filled with zeros. Finally, an  $N \times N \times N$  image was obtained via the inverse Fourier Transform. Along each **p**-space orientation,  $N$  evenly spaced image volumes were reconstructed. The 15 images on either end of any direction were discarded to ensure all images have sufficient DC signal. Consequently, a total of  $(N-30)$  images were used for each orientation. If the reconstruction of an image requires non-integer shift along any dimension, the **k**-space data were further upsampled by zero padding along that dimension in the image domain. For example, given the direction of  $[1 \ 3 \ 1]$ , one pixel shift in the second dimension requires a third of a pixel shift in the first and third dimension. To achieve this shift, the **k**-space was upsampled to a size of  $3N \times N \times 3N$ .

For each orientation, the standard deviation of the frequency and magnitude was computed. When computing the standard deviation of the frequency, the phase map at  $p = 0$  was subtracted from all images on a coil-by-coil basis. This subtraction removed both coil and background phases and did not require phase unwrapping. The resulting phase maps from all coils were then summed together. For the magnitude, images from all coils were combined *via* the square root of sum of the squares and normalized by that obtained at  $p = 0$ . To calculate the standard deviation of the dipole term, the frequency value at a given  $p$ -value was subtracted from that at  $-p$  and the resulting difference was divided by 2. To calculate the quadrupole term, the frequency at  $p$  was summed with that at  $-p$  and the resulting sum was divided by 2. Same procedures were applied for the magnitude. For each orientation, the  $p_{\max}$  value was recorded and used to compute the susceptibility tensors following Eqs. (7) and (8). A set of tensors was computed for each echo. Tensors from all echoes were combined to achieve optimal SNR using a weighted summation based on  $T_2^*$ -decay (Wu et al., 2012). The resulting tensors were diagonalized with eigenvalue decomposition.

## Results

### Simulation of axon bundles

We first verified the validity of the approach using a simulated bundle of parallel axons that was situated in a cubic voxel (Fig. 2a). Without noise, both magnitude and frequency showed a quadratic relationship with  $p$  as illustrated for five representative orientations (Figs. 2b and c). The linear term was absent due to the symmetry of the phantom and the properties of Fourier transform which state that the Fourier transform of an even function is even. While the magnitudes were similar among all directions, the frequency curves varied significantly, demonstrating clear anisotropy (Fig. 2c). Specifically, when the **p**-vector was parallel to the axons (direction 1:  $[0 \ 0 \ 1]$ ), the frequency stayed constant; when the **p**-vector was perpendicular to the axons (direction 5:  $[1 \ 0 \ 0]$ ), the frequency showed the largest variation. We computed the standard deviation of the magnitude and phase along each direction. We further illustrated this anisotropic property with a set of 3D color-coded glyphs (Fig. 2d). For each point on the surface of the glyph, the radial distance from that point to the origin was scaled by the standard deviation for the corresponding radial

direction. While the glyph of the magnitude appeared spherical ( $\delta m$  in Fig. 2d), the glyph of the frequency was donut-shaped ( $\delta f$  in Fig. 2d) with its inverse shaped like an elongated peanut ( $1/\delta f$  in Fig. 2d). From these glyphs, the orientation of the axons is easily identified by searching for the minimal standard deviation. In the case with SNR=20, we observed similar behaviors even though significant fluctuations were present in the signal curves and the glyphs (Figs. 2e–g).

From these standard deviations, we computed the quadrupole susceptibility tensor for the magnitude (denoted by  $\boldsymbol{\eta}_q$ ) and the frequency (denoted by  $\boldsymbol{\chi}_q$ ). The dipole susceptibility tensors ( $\boldsymbol{\eta}_d$  and  $\boldsymbol{\chi}_d$ ) were absent as there were no linear terms in the  $\mathbf{p}$ -space signal (Figs. 2b and c). The resulting tensors were decomposed with eigenvalue decomposition. The eigenvector corresponding to the minimal eigenvalue (minimal eigenvector for short) was along the  $z$ -axis for  $\boldsymbol{\chi}_q$ , the same orientation as the axons. However, for the magnitude, the minimal eigenvector of  $\boldsymbol{\eta}_q$  was long the  $y$ -axis. When noise was added, all eigenvalues increased. The fractional anisotropy (FA) of  $\boldsymbol{\chi}_q$  decreased from 0.727 to 0.155 while the FA of  $\boldsymbol{\eta}_q$  remains relatively constant at 0.005 (Table 1). FA was computed based on the three eigenvalues using the same formula as defined in DTI (Pierpaoli and Basser, 1996).

### p-Space STI of mouse brains ex vivo

Signal behavior of the mouse brain in the  $\mathbf{p}$ -space is shown in Fig. 3. Along any given orientation, neither the magnitude nor the frequency of gray matter showed significant dependence on the  $p$ -value (Fig. 3). White matter, on the other hand, demonstrated strong dependence on the  $p$ -value similar to the simulated axons. Specifically, both magnitude and frequency demonstrated increasing deviation from their values at the origin respectively with increasing  $p$ -values. These deviations were also orientation dependent. Unlike the simulation, however, the dependence in the mouse brains demonstrated both dipole and quadrupole relationship (Fig. 3). At the first echo (TE=4.4 ms), the SNR of the original images were 15.5 for white matter and 24.1 for gray matter; at the last echo (TE=15.0 ms), the SNR were 3.7 for white matter and 13.1 for gray matter. For each orientation, we computed the standard deviations of the dipole and quadrupole terms for the frequency ( $\delta f_d$  for dipole and  $\delta f_q$  for quadrupole) and the standard deviations for the magnitude ( $\delta m_d$  for dipole and  $\delta m_q$  for quadrupole).

For the frequency standard deviations, both the dipole and the quadrupole term showed clear anisotropy. Specifically, when the underlying fibers were parallel to the  $\mathbf{p}$ -vector, the dipole term  $\delta f_d$  was the smallest, e.g. in the hippocampus (hc) when  $\mathbf{p}=[1\ 0\ 0]$  and the genu corpus callosum (gcc) and the posterior part of the anterior commissure (acp) when  $\mathbf{p}=[0\ 1\ 0]$  (Fig. 4a). In particular, the acp nearly vanished when  $\mathbf{p}=[0\ 1\ 0]$  while it was the brightest when  $\mathbf{p}=[0\ 0\ 1]$  (Fig. 4a). Similar behaviors were observed for the quadrupole standard deviation  $\delta f_q$  (Supplementary Materials Fig. 1). From the 213 standard deviations, we further computed the dipole ( $\boldsymbol{\chi}_d$ ) and quadrupole ( $\boldsymbol{\chi}_q$ ) susceptibility tensor. The three eigenvalues of the dipole susceptibility tensor differed significantly from each other (Fig. 4b), confirming the anisotropy of the  $\mathbf{p}$ -space dipole tensor. To better visualize this anisotropy, we generated the glyph of  $1/\delta f_d$  for hc, gcc and acp (Fig. 4b). Similar to the findings in the simulation, the long axis of the glyph was parallel to the axon orientation. The fractional anisotropy in the white matter, though high (averaged around 0.6), did not provide good contrast between gray and white matter (Supplementary Materials Fig. 1). This reduced contrast was likely caused by the presence of noise as indicated by the simulation.

For the magnitude, while the standard deviation of the dipole term ( $\delta m_d$ ) exhibited similar anisotropic property as the frequency (Supplementary Materials Fig. 1), the quadrupole term ( $\delta m_q$ ) had low anisotropy (Fig. 4c). This low anisotropy was also apparent from the three

comparable eigenvalues of the quadrupole susceptibility tensor ( $\eta_q$ ) (Fig. 4d). Nevertheless, the quadrupole term provided strong contrast between gray and white matter (Figs. 4c and d). Interestingly, although the FA of the quadrupole tensor was low (less than 0.2), it still offered excellent contrast between gray and white matter (Supplementary Materials Fig. 1). This contrast did not appear to be affected by the noise as much as in the case of frequency, which was consistent with the findings in the simulation (Table 1).

To illustrate the orientation of the minimal eigenvector of the dipole susceptibility tensor  $\chi_d$ , we color-coded the orientations and scaled the color intensity by the trace of the tensor. The color scheme was: red representing left-right, green representing anterior–posterior and blue representing dorsal–ventral (Fig. 5a). The orientations were coherent within white matter fiber bundles, for example, the genu of corpus callosum (gcc), the anterior commissure (ac), the hippocampus (hc), and the trigeminal tracts (tt) (Fig. 5). The orientations also appeared to be consistent with the underlying axon orientation. For example, the gcc appeared mainly red as it connects the right and left hemisphere. The laminated structure of the commissure of superior colliculus (csc) was clear visible, interconnecting the superior colliculi on either side. In the pons and the medulla, the trigeminal tract was mainly green as it runs anterior–posterior direction. Due to tissue air boundaries, some artifacts were also visible at edges of the brain, e.g. in the olfactory bulb (Fig. 5a). These artifacts can be reduced with improved field shimming. The orientation maps of the minimal eigenvectors were similar for  $\chi_d$ ,  $\chi_q$  and  $\eta_d$  (Supplementary Materials Fig. 1). The orientation map of  $\eta_q$ , on the other hand, was different and not indicative of fiber orientation. These findings were consistent with the simulation.

A comparison between the minimal eigenvector of the dipole susceptibility tensor  $\chi_d$  and the major eigenvector of diffusion tensor was shown in Fig. 6. While overall the color maps appeared to be similar, differences were also observed. When the eigenvector of  $\chi_d$  was scaled by its trace (Fig. 6a), some structures were highlighted that were not clearly visible when the eigenvector was scaled by DTI FA (Fig. 6b), including, for example, the dentate gyrus (dg), the csc and one layered cortical structure. Similarly, none of these structures were present in the corresponding DTI maps (Fig. 6c). The angles between the two eigenvectors were generally smaller in white matter regions (Fig. 6d). The mean angle in regions with a DTI FA value larger than 0.35 was  $22^\circ \pm 13^\circ$ . Interestingly, the orientations within the cortical layer were similar between dipole susceptibility tensor and diffusion tensor (Fig. 6d), even though the structure was not visible in DTI (Fig. 6c).

### p-Space STI of human brain in vivo

At the first echo (TE=4.0 ms), the SNR of the human brain images were 80.1 for white matter and 75.1 for gray matter; at the last echo (TE=38.56 ms), the SNR were 35.6 for white matter and 34.0 for gray matter. Similar to the simulation and the mouse brains, the signal in the human brain white matter also varied significantly as a function of the  $p$ -value while the gray matter stayed relatively constant (Supplementary Materials Fig. 2).

For the dipole terms, the inverse of the standard deviations (i.e.  $1/\delta m_d$  and  $1/\delta f_d$ ) showed a clear dependence on the orientation of the  $\mathbf{p}$ -vector (Fig. 7a). When the axons were parallel to the  $\mathbf{p}$ -vector, both  $1/\delta m_d$  and  $1/\delta f_d$  were the largest in the corresponding white matter regions such as the posterior corona radiata (pcr) at  $\mathbf{p}=[1\ 0\ 0]$  and the splenium of the corpus callosum (scc) at  $\mathbf{p}=[0\ 1\ 0]$  (Fig. 7a). In other words, when the axons were parallel to the  $\mathbf{p}$ -vector,  $\delta m_d$  and  $\delta f_d$  were the smallest (Supplementary Materials Fig. 3). Based on this anisotropy, we computed the dipole susceptibility tensors ( $\chi_d$  in Fig. 7b and  $\eta_d$  in Supplementary Materials Fig. 3). The orientation of the minimal eigenvector was color-coded with red representing red-left, green representing anterior–posterior and blue

representing superior–inferior (Fig. 7b). The FA appeared noisy and did not provide good gray and white matter contrast (Supplementary Materials Fig. 3). The FA was also susceptible to large field inhomogeneity caused by air–tissue interfaces, for example, in areas near the sinus. To examine eigenvectors in the white matter, we thus chose to weigh the color intensity by the product of the fractional anisotropy and a T1-weighted image. The color map demonstrated a clear heterogeneity of eigenvector orientations within white matter fiber bundles. For example, the body of the corpus callosum indicated a right–left direction (red) while the pcr indicated an anterior–posterior direction (green) confirming the anisotropy observed in the standard deviation map. Finally, the orientations were consistent between the two dipole tensors (Fig. 7b and Supplementary Materials Fig. 3).

For the quadrupole terms, only the frequency demonstrated significant anisotropy (Fig. 7c). The magnitude showed weak anisotropy (Fig. 7c) but excellent tissue contrast, which was consistent with the mouse brain experiments. Specifically, the contrast exhibited by  $1/\delta m_q$  resembled that of a T<sub>2</sub>-weighted image (Fig. 7c). We then computed the quadrupole tensors for both the frequency (Fig. 7d) and the magnitude (Supplementary Materials Fig. 3). For the frequency, the trace and the orientation of its minimal eigenvector were similar to those of the dipole tensors (Fig. 7d). For the magnitude, the orientation of the minimal quadrupole eigenvector differed completely from the dipole tensors (Supplementary Materials Fig. 3). While the quadrupole tensor of the magnitude did not show any correlation with the fiber orientation, the quadrupole tensor of the frequency demonstrated a clear indication of underlying fiber structures. These findings were again consistent with the simulation and the *ex vivo* experiments.

## Discussion

At high fields, the weak interaction between magnetic fields and biological molecules is sufficiently strong to create a frequency shift in the Larmor frequency of nearby nuclear spins. Despite the paramount importance that frequency shift has attained in NMR, the utilization of frequency shift in MRI has been very limited. While measuring frequency shift and its anisotropy has enabled NMR to determine structures of large molecules, MRI has not been able to routinely utilize the vast information existed in the frequency. Yet, the similarity between the frequency shift caused by the atomic arrangement in a large molecule and that by an ordered cellular architecture cannot be overlooked. The **p**-space STI method developed here provides MRI a means to image this higher order frequency information and utilize it to elucidate tissue microstructure. The method requires only a single acquisition of 3D gradient-recalled-echo images. It also allows high spatial resolution. A notable advantage of the method is the ability to image anisotropic susceptibility tensors *in vivo* without rotating the object or the magnetic field. Although considerable work remains to be done to improve the accuracy of the tools developed here, we expect the **p**-space method to open a new avenue for studying tissue microstructure in general and brain connectivity in particular.

The ability to quantify anisotropic tissue property with a single image acquisition was made possible by sampling and analyzing the **p**-space signal. The **p**-space can be sampled by applying a pulsed field gradient prior to data acquisition, or equivalently, by shifting the acquired **k**-space data by a desired **p**-vector. To maintain overall signal consistency, the central **k**-space signal (the DC signal) should not be shifted outside the reconstruction window. As a result, the *p*-value applied along any direction should be well within the range of  $\pm 0.5$ . On the other hand, the more orientations are sampled in the **p**-space, the more accurate the susceptibility tensors can be estimated. The gain in signal-to-noise ratio (SNR), however, does not increase linearly with the number of orientations. This restriction is due to the correlated noise among **p**-space images that are reconstructed from the same raw data.

In this study, we used 213 orientations which was a good tradeoff between computational efficiency and SNR. The shifted reconstruction required zero-filling of the unsampled  $\mathbf{k}$ -space. Zero-filling in the  $\mathbf{k}$ -space introduced a known rippling artifact in the image space which was visible in some  $\mathbf{p}$ -space images (Figs. 3 and 7). Such artifacts could be suppressed with a more optimally designed windowing function rather than the simple step function associated with zero-filling. Nevertheless, comparison with fully sampled  $\mathbf{k}$ -space data (i.e.  $\mathbf{p}$ -space images were reconstructed at an  $N/2$  matrix) showed that this zero-filling did not introduce appreciable errors in the multipole tensors. This is likely due to the large number of orientations used which effectively suppressed the rippling artifact.

Analyzing the signal variations among  $\mathbf{p}$ -space directions allowed us to determine a set of dipole ( $\chi_d$  and  $\eta_d$ ) and quadrupole ( $\chi_q$  and  $\eta_q$ ) susceptibility tensors. These four multipole tensors characterize higher-order anisotropic signal behavior in the  $\mathbf{p}$ -space while the conventional susceptibility tensor  $\chi$  characterizes the zero-th order frequency shift. The anisotropy of the conventional susceptibility tensor  $\chi$  describes the differential magnetic response at different field orientations. In contrast to the conventional susceptibility tensor, the  $\mathbf{p}$ -space multipole tensors describe the signal heterogeneity within one voxel at any given external field orientation. By expanding the  $\mathbf{p}$ -space signal with the Taylor's series, we projected higher-rank magnetic multipole tensors onto the direction of the external field. Although we only characterized the anisotropy with rank-2 tensors, the method can be readily extended to include tensors of higher ranks. In fact, higher ranks may be necessary to characterize more complex tissue structures, similar to the use of kurtosis and skewness tensors in diffusion MRI (Liu et al., 2004). The  $\mathbf{p}$ -space anisotropy may also be characterized in the spherical coordinate where the anisotropy can be described by a set of spherical harmonics (Jackson, 1975).

Multipole susceptibility tensors originate from sub-voxel tissue heterogeneity and structural asymmetry. If the magnetization is uniform within a voxel, there will be no phase terms in the  $\mathbf{p}$ -space signal based on the Fourier relationship (Eq. (2)). If the magnetization vectors are non-uniformly distributed, signal phase and thus multipole tensors are non-vanishing. If a voxel has completely symmetrical magnetization distribution (a low probability event), the odd terms, thus the dipole tensors, in the  $\mathbf{p}$ -space signal vanish. However, the quadrupole tensors still exist as they are derived from the even terms. The current work proposed and developed a practical method for imaging these anisotropic susceptibility tensors. A complete understanding of the relationship between these tensors, cellular organization and fiber orientations requires further investigation. Correlating the results with DTI may provide additional insights. In the simple case of parallel axons, we identified the minor eigenvectors of three susceptibility tensors were aligned with the axons. In these parallel fibers, we showed that anisotropy is high in simulation and in *ex vivo* imaging at 9.4 Tesla; however, anisotropy is reduced in the presence of noise especially in the *in vivo* case. As a result, anisotropy value did not provide high contrast between the gray matter and white matter *in vivo* at 3.0 Tesla. It is also likely that gray matter may exhibit intrinsic anisotropic multipole tensors due to their structural complexity, thus further contributing to the reduced contrast between gray and white matter in the human brain.

While the multipole tensors of the mouse brain measured at 9.4 Tesla were generally of high quality and provided excellent image contrast, the challenge of  $\mathbf{p}$ -space imaging of human brains *in vivo* at 3.0 Tesla remains to be fully resolved. At 3.0 Tesla, the field perturbation within a voxel is much smaller. The corresponding contrast between different tissue types and among fibers of different orientations is also reduced thus becoming more susceptible to noise contamination. For example, the contrast between gray and white matter is significantly smaller in the human data compared to the mouse data (Figs. 4 and 7). The agreement between the minimal eigenvector orientations and the underlying fiber

orientations is also reduced at 3.0 Tesla. For example, the cortical spinal tract has a mixture of green and blue colors and is not always consistent with the tract orientation (Figs. 7b and d). In addition, large field gradients introduced by tissue-air boundaries pose additional difficulties in the multipole tensor calculation as these gradients are not completely removed in the **p**-space processing. Residual gradients caused noticeable artifacts such as the dark region in the frontal lobe when the **p**-vector is in the [0 0 1] direction, i.e. parallel to the residual gradients (Fig. 7a). Future implementation of multipole susceptibility tensor imaging in the **p**-space will therefore greatly benefit from improved field shimming.

With the **p**-space method, probing brain microstructure *in vivo* may become possible at resolutions higher than what current MRI methods are capable of. Higher field strength will further extend the ability of the method to quantify susceptibility anisotropy. At higher field, each spin accrues more phase offsets (Duyn et al., 2007) thus increasing the signal range along any given and improving our ability to quantify higher-order anisotropy. Exploring the capability of the **p**-space method for imaging neuronal and muscular fiber connectivity could be of great interest for applications in which diffusion tensor imaging reaches its limits, such as imaging at high spatial resolution and at ultra-high field strength when tissue heating becomes problematic (Hoult and Phil, 2000; Vaughan et al., 2006). In the future, **p**-space STI could be implemented to study moving organs such as kidneys, livers, fetus brains and even beating hearts as gradient echo can be easily gated and far less sensitive to motion.

## Supplementary Material

Refer to Web version on PubMed Central for supplementary material.

## Acknowledgments

We thank G.A. Johnson for access to the 9.4T scanner at Duke Center for In Vivo Microscopy, Y. Qi, G. Cofer and R. Dibb for assistance in animal preparation and data acquisition. We thank A.W. Song and C. Petty of the Brain Imaging and Analysis Center for assistance with computing on the cluster.

## References

- Basser PJ, Mattiello J, LeBihan D. Estimation of the effective self-diffusion tensor from the NMR spin echo. *J Magn Reson B*. 1994; 103:247–254. [PubMed: 8019776]
- Basser PJ, Pajevic S, Pierpaoli C, Duda J, Aldroubi A. In vivo fiber tractography using DT-MRI data. *Magn Reson Med*. 2000; 44:625–632. [PubMed: 11025519]
- Cavalli A, Salvatella X, Dobson CM, Vendruscolo M. Protein structure determination from NMR chemical shifts. *Proc Natl Acad Sci U S A*. 2007; 104:9615–9620. [PubMed: 17535901]
- de Beer T, van Zuylen CW, Hard K, Boelens R, Kaptein R, Kamerling JP, Vliegthart JF. Rapid and simple approach for the NMR resonance assignment of the carbohydrate chains of an intact glycoprotein. Application of gradient-enhanced natural abundance <sup>1</sup>H-<sup>13</sup>C HSQC and HSQC-TOCSY to the alpha-subunit of human chorionic gonadotropin. *FEBS Lett*. 1994; 348:1–6. [PubMed: 8026573]
- de Rochefort L, Brown R, Prince MR, Wang Y. Quantitative MR susceptibility mapping using piecewise constant regularized inversion of the magnetic field. *Magn Reson Med*. 2008; 60:1003–1009. [PubMed: 18816834]
- Dixon WT. Simple proton spectroscopic imaging. *Radiology*. 1984; 153:189–194. [PubMed: 6089263]
- Duyn JH, van Gelderen P, Li TQ, de Zwart JA, Koretsky AP, Fukunaga M. High-field MRI of brain cortical substructure based on signal phase. *Proc Natl Acad Sci U S A*. 2007; 104:11796–11801. [PubMed: 17586684]
- Glover GH, Schneider E. Three-point Dixon technique for true water/fat decomposition with B0 inhomogeneity correction. *Magn Reson Med*. 1991; 18:371–383. [PubMed: 2046518]

- Haacke EM, Lai S, Yablonskiy DA, Lin W. In vivo validation of the bold mechanism: a review of signal changes in gradient echo functional MRI in the presence of flow. *Int J Imaging Syst Technol.* 1995; 6:153–163.
- He X, Yablonskiy DA. Biophysical mechanisms of phase contrast in gradient echo MRI. *Proc Natl Acad Sci U S A.* 2009; 106:13558–13563. [PubMed: 19628691]
- Hoult DI, Phil D. Sensitivity and power deposition in a high-field imaging experiment. *J Magn Reson Imaging.* 2000; 12:46–67. [PubMed: 10931564]
- Jackson, JD. *Classical Electrodynamics.* 2. John Wiley & Sons, Inc; 1975.
- Johnson GA, Cofer GP, Gewalt SL, Hedlund LW. Morphologic phenotyping with MR microscopy: the visible mouse. *Radiology.* 2002; 222:789–793. [PubMed: 11867802]
- Lauterbur PC. Image formation by induced local interactions: examples employing nuclear magnetic resonance. *Nature.* 1973; 242:190–191.
- Lee J, Shmueli K, Fukunaga M, van Gelderen P, Merkle H, Silva AC, Duyn JH. Sensitivity of MRI resonance frequency to the orientation of brain tissue microstructure. *Proc Natl Acad Sci U S A.* 2010; 107:5130–5135. [PubMed: 20202922]
- Li L. Magnetic susceptibility quantification for arbitrarily shaped objects in inhomogeneous fields. *Magn Reson Med.* 2001; 46:907–916. [PubMed: 11675642]
- Li W, Wu B, Liu C. Quantitative susceptibility mapping of human brain reflects spatial variation in tissue composition. *Neuroimage.* 2011; 55:1645–1656. [PubMed: 21224002]
- Li W, Wu B, Avram AV, Liu C. Magnetic susceptibility anisotropy of human brain in vivo and its molecular underpinnings. *Neuroimage.* 2012a; 59:2088–2097. [PubMed: 22036681]
- Li X, Vikram DS, Lim IA, Jones CK, Farrell JA, van Zijl PC. Mapping magnetic susceptibility anisotropies of white matter in vivo in the human brain at 7T. *Neuroimage.* 2012b; 62:314–330. [PubMed: 22561358]
- Liu C. Susceptibility tensor imaging. *Magn Reson Med.* 2010; 63:1471–1477. [PubMed: 20512849]
- Liu C, Bammer R, Acar B, Moseley ME. Characterizing non-Gaussian diffusion by using generalized diffusion tensors. *Magn Reson Med.* 2004; 51:924–937. [PubMed: 15122674]
- Liu C, Li W, Wu B, Jiang Y, Johnson GA. 3D fiber tractography with susceptibility tensor imaging. *Neuroimage.* 2012; 59:1290–1298. [PubMed: 21867759]
- Moseley ME, Cohen Y, Kucharczyk J, Mintorovitch J, Asgari HS, Wendland MF, Tsuruda J, Norman D. Diffusion-weighted MR imaging of anisotropic water diffusion in cat central nervous system. *Radiology.* 1990; 176:439–445. [PubMed: 2367658]
- Otting G, Qian YQ, Billeter M, Muller M, Affolter M, Gehring WJ, Wuthrich K. Protein–DNA contacts in the structure of a homeodomain–DNA complex determined by nuclear magnetic resonance spectroscopy in solution. *EMBO J.* 1990; 9:3085–3092. [PubMed: 1976507]
- Pierpaoli C, Basser PJ. Toward a quantitative assessment of diffusion anisotropy. *Magn Reson Med.* 1996; 36:893–906. [PubMed: 8946355]
- Rauscher A, Sedlacik J, Barth M, Mentzel HJ, Reichenbach JR. Magnetic susceptibility-weighted MR phase imaging of the human brain. *AJNR Am J Neuroradiol.* 2005; 26:736–742. [PubMed: 15814914]
- Salomir R, Denis de Senneville B, Moonen CTW. A fast calculation method for magnetic field inhomogeneity due to an arbitrary distribution of bulk susceptibility. *Concepts Magn Reson B.* 2003; 19B:26–34.
- Tolman JR, Flanagan JM, Kennedy MA, Prestegard JH. Nuclear magnetic dipole interactions in field-oriented proteins: information for structure determination in solution. *Proc Natl Acad Sci U S A.* 1995; 92:9279–9283. [PubMed: 7568117]
- van Zijl P, Ruessink B, Bulthuis J, MacLean C. NMR of partially aligned liquids: magnetic susceptibility anisotropies and dielectric properties. *Acc Chem Res.* 1984; 17:172–180.
- Vaughan T, DelaBarre L, Snyder C, Tian J, Akgun C, Shrivastava D, Liu W, Olson C, Adriany G, Strupp J, Andersen P, Gopinath A, van de Moortele PF, Garwood M, Ugurbil K. 9.4T human MRI: preliminary results. *Magn Reson Med.* 2006; 56:1274–1282. [PubMed: 17075852]
- Weisskoff RM, Kiihne S. MRI susceptometry: image-based measurement of absolute susceptibility of MR contrast agents and human blood. *Magn Reson Med.* 1992; 24:375–383. [PubMed: 1569876]

Wishart DS, Sykes BD, Richards FM. The chemical shift index: a fast and simple method for the assignment of protein secondary structure through NMR spectroscopy. *Biochemistry*. 1992; 31:1647–1651. [PubMed: 1737021]

Wu B, Li W, Avram AV, Gho SM, Liu C. Fast and tissue-optimized mapping of magnetic susceptibility and T2\* with multi-echo and multi-shot spirals. *Neuroimage*. 2012; 59:297–305. [PubMed: 21784162]

## Appendix A

In a Cartesian coordinate, the phase of the  $\mathbf{p}$ -space signal,  $\Phi(\mathbf{r}, \mathbf{p})$ , can be expanded in a Taylor's series with respect to  $\mathbf{p}$  as follows,

$$\Phi(\mathbf{r}, \mathbf{p}) = \sum_{n=0}^{\infty} \frac{1}{n!} (\mathbf{p} \cdot \nabla_{\mathbf{p}'})^n \Phi(\mathbf{r}, \mathbf{p}') \Big|_{\mathbf{p}'=0} \quad (\text{A.1})$$

Keeping terms up to the second order ( $n=2$ ), Eq. (A.1) can be rewritten as

$$\Phi(\mathbf{r}, \mathbf{p}) = \Phi_0(\mathbf{r}) + \widehat{p}_i \Phi'_{i}(\mathbf{r}) p + \frac{1}{2} \widehat{p}_i \widehat{p}_j \Phi''_{ij}(\mathbf{r}) p^2 \quad (\text{A.2})$$

Here,  $\widehat{\mathbf{p}}$  is the unit directional vector and  $\Phi'_{i}$  is the first-order partial derivative with respect to  $p_i$ . Einstein's summation convention is used in Eq. (A.2). That is, summation over all possible values is assumed for repeated index variables. Analogous to the multipole expansion of the electromagnetic potentials (both electric scalar potential and magnetic vector potential), these three terms correspond to a monopole, a dipole and a quadrupole respectively. The next order of multipole that is omitted here is called octupole. Alternatively, the expansion can also be expressed in a spherical coordinate where the orthonormal spherical harmonics are used as the basis function.

The monopole term ( $n=0$ ) denoted as  $\Phi_0(\mathbf{r}) = \Phi(\mathbf{r}, \mathbf{p}'=0)$  is the mean phase of the voxel at position  $\mathbf{r}$ . It is related to the image-space dipole susceptibility tensor (rank 2)  $\chi(\mathbf{r})$  following (Liu, 2010)

$$\Phi_0(\mathbf{r}) = \gamma t FT^{-1} \left\{ \frac{1}{3} \widehat{\mathbf{B}}_0 FT \{ \chi(\mathbf{r}) \} \mathbf{B}_0 - k_3 \frac{\mathbf{k}^T FT \{ \chi(\mathbf{r}) \} \mathbf{B}_0}{k^2} \right\} \quad (\text{A.3})$$

Here,  $\widehat{\mathbf{B}}_0$  is a unit directional vector (dimensionless) corresponding to the magnetic flux density  $\mathbf{B}_0$ .

The dipole term ( $n=1$ ), though defined by a vector  $\Phi'_{i}$ , can be expressed more generally in terms of a rank-2 dipole susceptibility tensor as

$$\Phi_d = \gamma B_0 \widehat{\mathbf{p}}^T \chi_d(\mathbf{r}) \widehat{\mathbf{p}} \quad (\text{A.4})$$

This expression is identical to the dipole term in Eq. (A.2) when the off-diagonal elements of the rank-2 tensor  $\chi_d$  are zero. However, due to the truncation of the Taylor's series, the off-diagonal elements may not be zero in practice.

The quadrupole term ( $n=2$ ) can be expressed in terms of a quadrupole susceptibility tensor  $\chi_q$  as follows,

$$\Phi_q(\mathbf{r}, \mathbf{p}) = \gamma B_0 t \widehat{\mathbf{p}}^T \chi_q(\mathbf{r}) \widehat{\mathbf{p}} p^2 \quad (\text{A.5})$$

Comparing to Eq. (A.2), it is easy to see that

$$\Phi''_{ij}(\mathbf{r}) = 2\gamma B_0 t \chi_{q,ij} \quad (\text{A.6})$$

Combining Eqs. (A.2), (A.4) and (A.5), one obtains

$$\Phi(\mathbf{p}) = \Phi_0 + \gamma B_0 t \widehat{\mathbf{p}}^T \chi_d \widehat{\mathbf{p}} p + \gamma B_0 t \widehat{\mathbf{p}}^T \chi_q \widehat{\mathbf{p}} p^2 \quad (\text{A.7})$$

Similarly, the magnitude can also be expanded in a Taylor's series as

$$m(\mathbf{p}) = m_0 \left( 1 + \gamma B_0 t \widehat{\mathbf{p}}^T \boldsymbol{\eta}_d \widehat{\mathbf{p}} p + \gamma B_0 t \widehat{\mathbf{p}}^T \boldsymbol{\eta}_q \widehat{\mathbf{p}} p^2 \right) \quad (\text{A.8})$$

where both  $\boldsymbol{\eta}_d$  and  $\boldsymbol{\eta}_q$  are dimensionless rank-2 tensors.

## Appendix B

The mean phase of the dipolar term,  $\bar{\Phi}_d$ , is zero. The mean phase of the quadrupolar term along the unit-direction  $\widehat{\mathbf{p}}$  can be derived as follows

$$\begin{aligned} \bar{\Phi}_q &= \frac{1}{2p_{\max}} \int_{-p_{\max}}^{p_{\max}} \gamma B_0 t \widehat{\mathbf{p}}^T \chi_q \widehat{\mathbf{p}} p^2 dp \\ &= \frac{1}{2p_{\max}} \gamma B_0 t \widehat{\mathbf{p}}^T \chi_q \widehat{\mathbf{p}} \int_{-p_{\max}}^{p_{\max}} p^2 dp \\ &= \frac{1}{3} \gamma B_0 t p_{\max}^2 \widehat{\mathbf{p}}^T \chi_q \widehat{\mathbf{p}} \end{aligned} \quad (\text{B.1})$$

The mean of the squared phase is derived as

$$\begin{aligned} \overline{\Phi_d^2} &= \frac{1}{2p_{\max}} \int_{-p_{\max}}^{p_{\max}} (\gamma B_0 t \widehat{\mathbf{p}}^T \chi_d \widehat{\mathbf{p}} p)^2 dp \\ &= \frac{1}{3} (\gamma B_0 t p_{\max} \widehat{\mathbf{p}}^T \chi_d \widehat{\mathbf{p}})^2 \end{aligned} \quad (\text{B.2})$$

$$\begin{aligned} \overline{\Phi_q^2} &= \frac{1}{2p_{\max}} \int_{-p_{\max}}^{p_{\max}} (\gamma B_0 t \widehat{\mathbf{p}}^T \chi_q \widehat{\mathbf{p}} p^2)^2 dp \\ &= \frac{1}{5} (\gamma B_0 t p_{\max}^2 \widehat{\mathbf{p}}^T \chi_q \widehat{\mathbf{p}})^2 \end{aligned} \quad (\text{B.3})$$

Therefore, the variances are given by

$$\delta\Phi_d^2 = \overline{\Phi_d^2} - \bar{\Phi}_d^2 = \frac{1}{3} (\gamma B_0 t p_{\max} \widehat{\mathbf{p}}^T \chi_d \widehat{\mathbf{p}})^2 \quad (\text{B.4})$$

$$\delta\Phi_q^2 = \overline{\Phi_q^2} - \bar{\Phi}_q^2 = \frac{4}{45} (\gamma B_0 t p_{\max}^2 \widehat{\mathbf{p}}^T \chi_q \widehat{\mathbf{p}})^2 \quad (\text{B.5})$$

## Appendix C. Supplementary data

Supplementary data to this article can be found online at <http://dx.doi.org/10.1016/j.neuroimage.2012.10.050>.

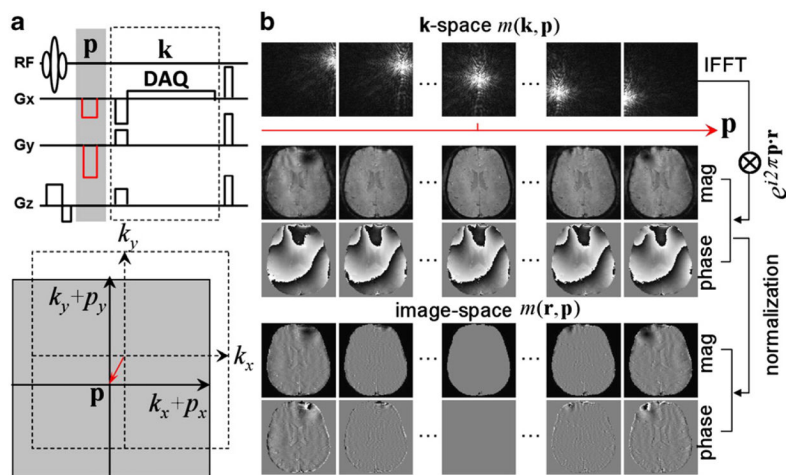


**Fig. 1.**

Flowchart for constructing the **p**-space. (a) MRI pulse sequence for sampling the **p**-space which can be achieved by applying pulsed field gradients or by shifting **k**-space data. Gradients for sampling the **p**-space and the corresponding **p**-vector are drawn in red. These gradients can be varied to achieve different **p**-vector. Since these gradients simply cause shifts in the **k**-space, these shifts can be achieved easily in post-processing without actually applying the physical gradients. Sampling of the **k**-space is achieved by the data acquisition gradient G<sub>x</sub> (DAQ) and phase encoding gradients G<sub>y</sub> and G<sub>z</sub>. (b) Basic steps of analyzing **p**-space signal. At each location in the **p**-space, a complex image is reconstructed by inverse Fast Fourier Transform (IFFT). A linear phase is removed from the image. The magnitude and phase images are then normalized by those at  $\mathbf{p}=0$  via division and subtraction respectively. (For interpretation of the references to color in this figure legend, the reader is referred to the web version of this article.)

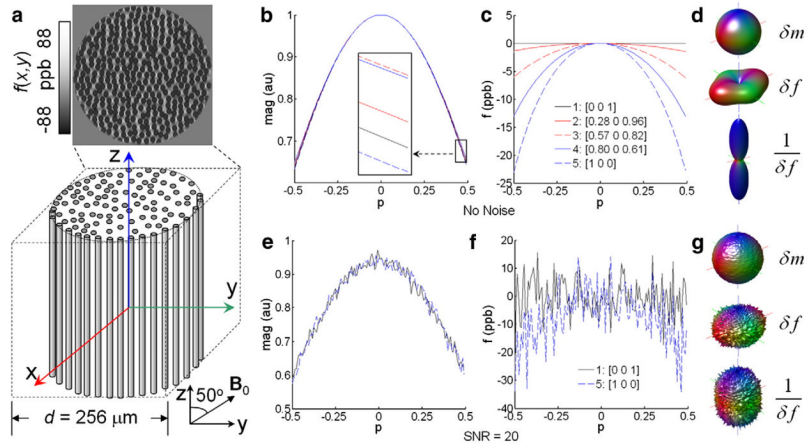


**Fig. 2.** Analysis of a simulated bundle of parallel axons in the  $\mathbf{p}$ -space. (a) A schematic representation of the axonal bundle and the frequency distribution in the axial plane. Two scenarios were evaluated: one without noise (b–d) and the other with SNR=20 (e–g). (b) Magnitude profile along five  $\mathbf{p}$ -space orientations showing small orientation dependence. (c) Frequency profile along the same five orientations showing significant orientation variations. The largest  $p$ -value dependence was found at direction 5 when the  $\mathbf{p}$ -vector was perpendicular to the axons. (d) Surface rendering (glyph) of the orientation distribution for the standard deviations of magnitude and frequency. The orientation of the axons can be clearly identified from the frequency glyphs as the minimum in  $\delta f$  and maximum in  $1/\delta f$ . Similar results were found for SNR=20 (e–g). Color coding of the glyphs was as follows: red representing the  $x$ -axis, green representing the  $y$ -axis and blue representing the  $z$ -axis. (For interpretation of the references to color in this figure legend, the reader is referred to the web version of this article.)

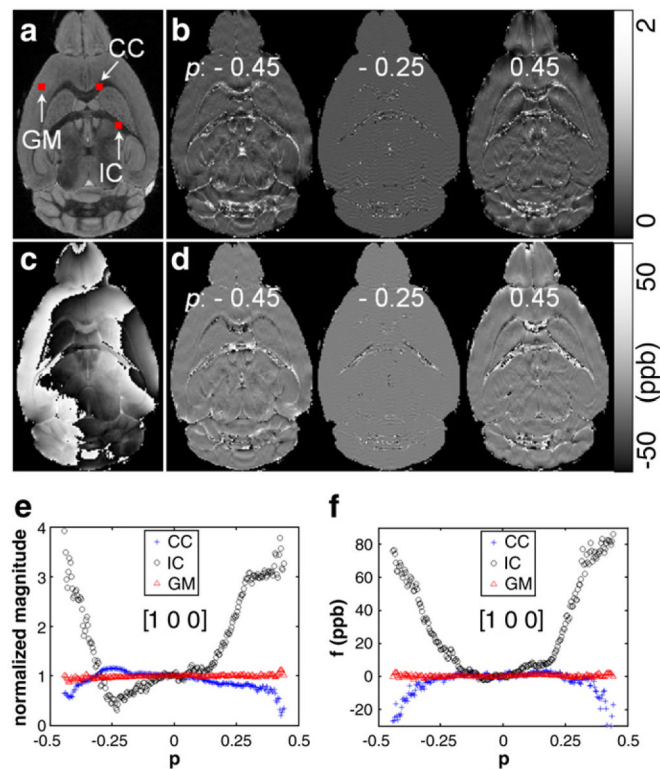


**Fig. 3.**

Signal behavior of mouse brain in the  $\mathbf{p}$ -space. (a) A representative magnitude image at  $p=0$ . (b) Three normalized magnitude images at  $p=-0.45$ ,  $-0.25$  and  $0.45$  respectively with the  $\mathbf{p}$ -vector along the  $x$ -axis (vertical). Increased contrast was seen at larger  $p$ -values. (c) Corresponding phase image at  $p=0$ . (d) Corresponding normalized frequency images at  $p=-0.45$ ,  $-0.25$  and  $0.45$  respectively. Increased contrast was seen at larger  $p$ -values similar to the magnitude. (e) Normalized magnitude as a function of the  $p$ -value in the corpus callosum (CC), internal capsule (IC) and gray matter (GM). The voxel locations were shown in (a). (f) Normalized frequency as a function of the  $p$ -value in the same three voxels. While little  $p$ -value dependence was observed in the gray matter, significant dependence was evident in the white matter for both magnitude and frequency. (For interpretation of the references to color in this figure legend, the reader is referred to the web version of this article.)

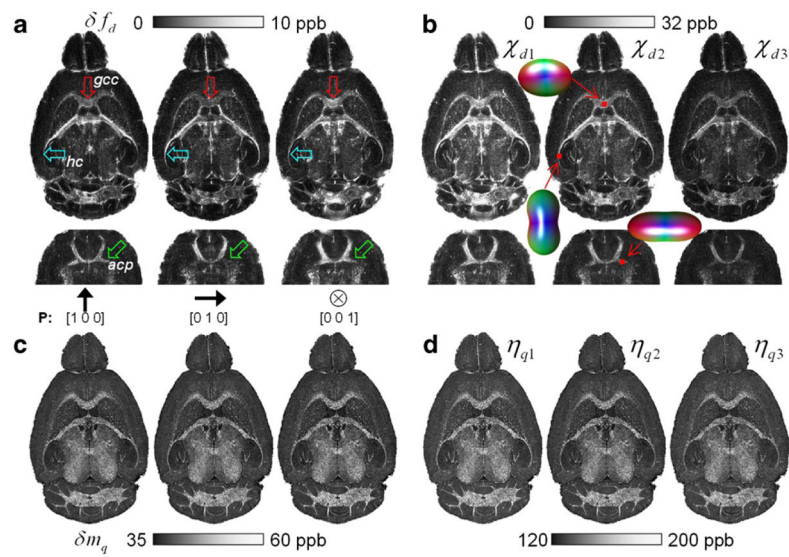


**Fig. 4.** Representative multipoles computed from dipole frequency and quadrupole magnitude. (a) Standard deviations of the dipole frequency along three orthogonal  $\mathbf{p}$ -space orientations: [1 0 0], [0 1 0] and [0 0 1]. The contrast within the white matter showed clear orientation dependence (arrows). gcc — genu of corpus callosum; hc — hippocampus; acp —posterior portion of anterior commissure. (b) Eigenvalues of the dipole susceptibility tensor computed from the frequency. Anisotropy was evident from the differences in the eigenvalues and the elongated glyphs in the gcc, hc and acp. The glyphs were constructed based on  $1/\delta f_d$  as in Fig. 2. (c) Standard deviations of the quadrupole magnitude did not show significant orientation variations among the three directions. (d) Eigenvalues of the quadrupole susceptibility tensor computed from the magnitude did not show significant differences. However, they provided high contrast between gray and white matter. The magnitude was normalized by that at  $p=0$ . (For interpretation of the references to color in this figure legend, the reader is referred to the web version of this article.)

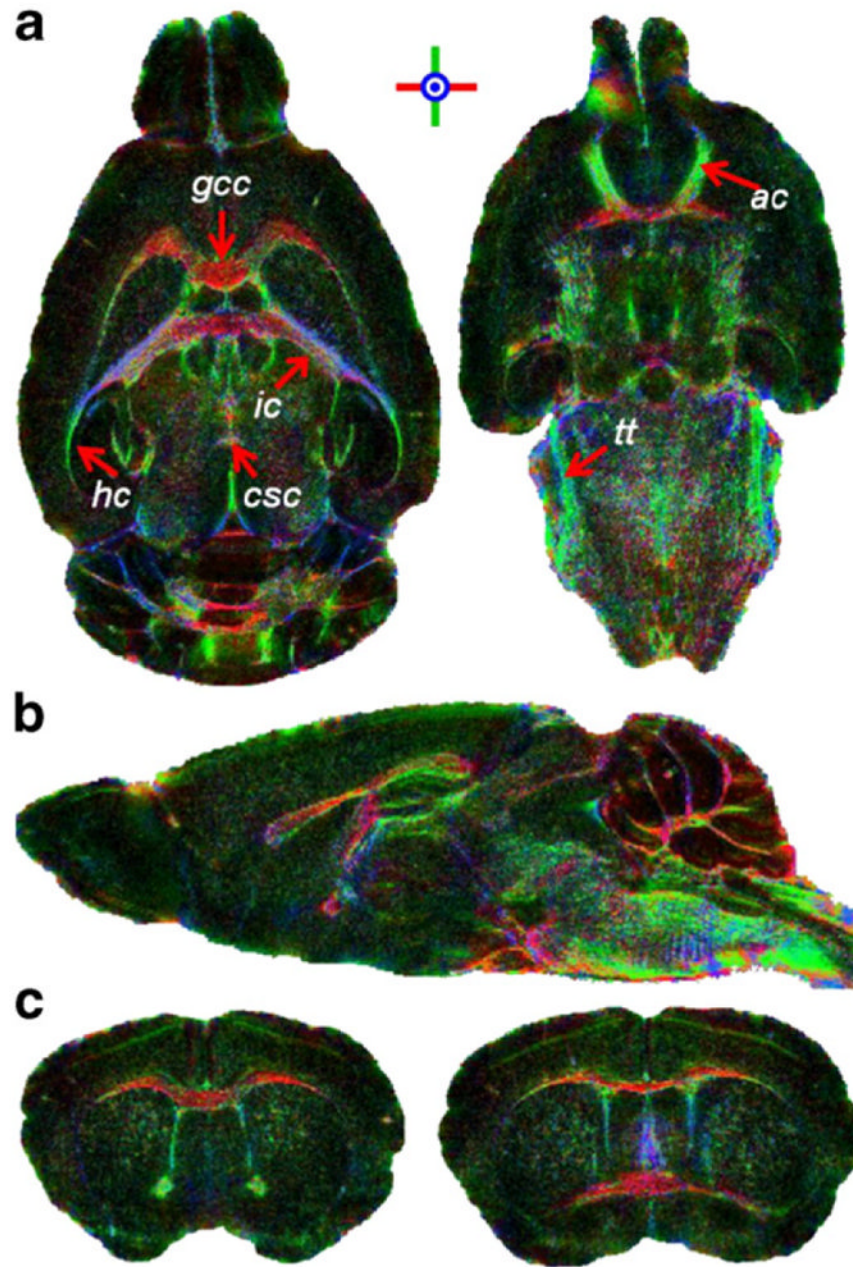


**Fig. 5.** Eigenvector orientation of dipole susceptibility tensor in the white matter of mouse brain. (a) Two representative axial slices of color-coded minor eigenvector of dipole susceptibility tensor  $\chi_d$ . Color schemes were: red representing left-right, green representing anterior-posterior and blue representing dorsal-ventral. Orientations of major fiber tracts could be identified. gcc — genu of corpus callosum; ic — internal capsule; hc — hippocampus; csc — commissure of superior colliculus; ac — anterior commissure; tt — trigeminal tract. (b) A representative sagittal slice. (c) Two coronal slices of the same brain. (For interpretation of the references to color in this figure legend, the reader is referred to the web version of this article.)

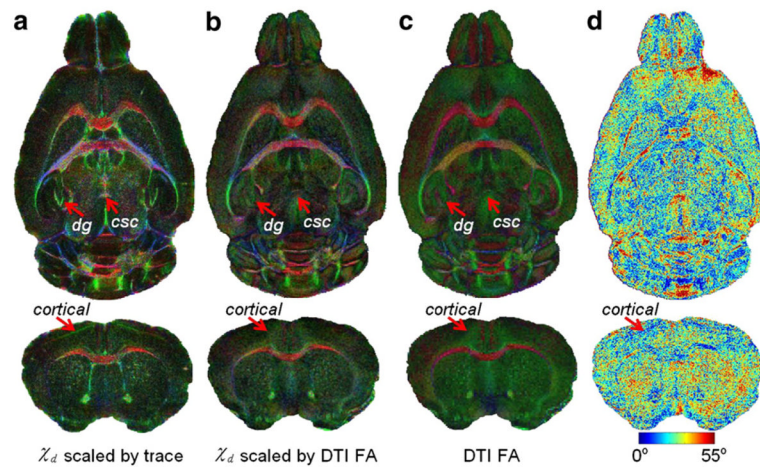


**Fig. 6.**

Comparison of eigenvector orientations between dipole susceptibility tensor  $\chi_d$  and diffusion tensor. (a) Orientations of the minimal eigenvector of dipole susceptibility tensor weighted by its trace. A layered cortical structure was visible in the coronal slice. dg — dentate gyrus. (b) Orientations of the minimal eigenvector of dipole susceptibility tensor weighted by DTI FA. (c) Orientations of the major eigenvector of diffusion tensor weighted by its FA. (d) Maps of angles between the minimal eigenvector of  $\chi_d$  and the major eigenvector of the diffusion tensor. Smaller angles were observed in the white matter. (For interpretation of the references to color in this figure legend, the reader is referred to the web version of this article.)

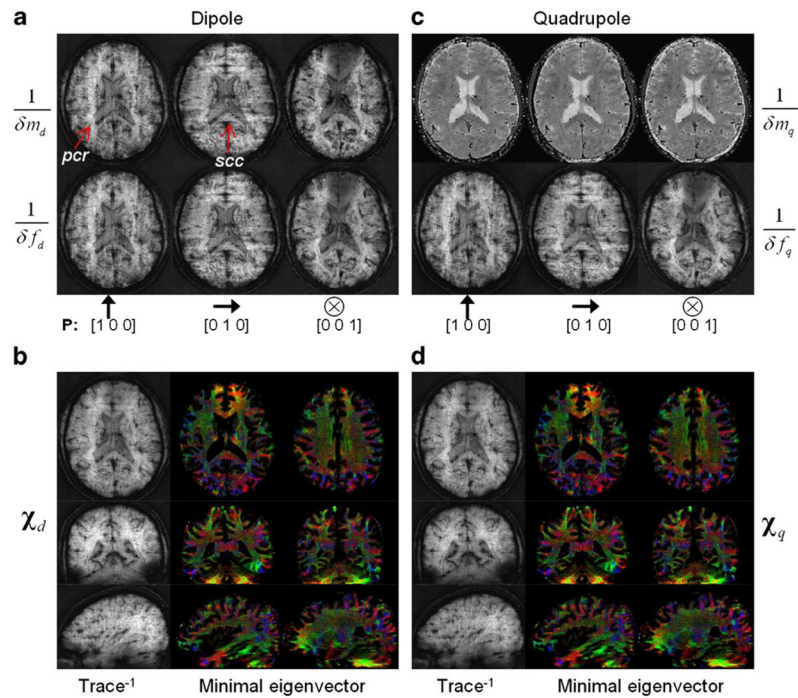


**Fig. 7.** Multipole susceptibility tensor imaging of human brain *in vivo*. (a) Inverse standard deviations of the dipole magnitude and dipole frequency along three orthogonal orientations. White matter contrast is clearly orientation dependent, e.g. in the pcr and scc. pcr — posterior corona radiata; scc — splenium of the corpus callosum. (b) Inverse trace of the dipole susceptibility tensor  $\chi_d$  and color-coded minor eigenvectors in the axial, coronal and sagittal planes. (c) Inverse standard deviations of the quadrupole magnitude and frequency along three orthogonal orientations. White matter contrast is orientation dependent for the quadrupole frequency but not for the quadrupole magnitude. (d) Inverse trace of the quadrupole susceptibility tensor  $\chi_q$  and color-coded minor eigenvectors in the axial, coronal and sagittal planes. In the axial planes, color schemes were: red representing left-right, green representing anterior-posterior and blue representing superior-inferior. (For interpretation of the references to color in this figure legend, the reader is referred to the web version of this article.)

Table 1

Quadrupole susceptibility tensors of simulated axons.

	Noise Free		SNR=20		Eval	FA
	Evec	Eval	FA	Evec		
$\chi_a$ (ppb)	[0 0 1]	1.3	0.727	[0 0 1]	87.2	0.155
	[0 1 0]	66.7		[0.08 0.996 0.0]	110.5	
	[1 0 0]	82.0		[0.996 -0.085 0.0]	119.0	
$\eta_b$ (ppb)	[0 0 1]	508	0.005	[0.046 0.037 0.998]	513	0.005
	[1 0 0]	504		[0.997 -0.06 -0.044]	508	
	[0 1 0]	509		[0.058 0.998 -0.04]	513	

Note: Evec — eigenvector; Eval — eigenvalue; FA — fractional anisotropy.